THE EUROPEAN
PHYSICAL JOURNAL C

Check for
updates

Regular Article - Experimental Physics

Probing gauge-Higgs unification models at the ILC with quark–antiquark forward–backward asymmetry at center-of-mass energies above the Z mass

A. Irles[1,a] , **J. P. Márquez**[1], **R. Pöschl**[2], **F. Richard**[2], **A. Saibel**[1], **H. Yamamoto**[1], **N. Yamatsu**[3,4]

[1] IFIC, Universitat de València and CSIC, C./ Catedrático José Beltrán 2, 46980 Paterna, Spain
[2] Université Paris-Saclay, CNRS/IN2P3, IJCLab, 91405 Orsay, France
[3] Department of Physics, National Taiwan University, Taipei 10617, Taiwan, ROC
[4] Yukawa Institute for Theoretical Physics, Kyoto University, Kitashirakawa Oiwakecho, Sakyo-ku, Kyoto 606-8502, Japan

Abstract The International Linear Collider (ILC) will allow the precise study of $e^-e^+ \rightarrow q\bar{q}$ interactions at different center-of-mass energies from the Z-pole to 1 TeV. In this paper, we discuss the experimental prospects for measuring differential observables in $e^-e^+ \rightarrow b\bar{b}$ and $e^-e^+ \rightarrow c\bar{c}$ at the ILC baseline energies, 250 and 500 GeV. The study is based on full simulation and reconstruction of the International Large Detector (ILD) concept. Two gauge-Higgs unification models predicting new high-mass resonances beyond the Standard Model are discussed. These models predict sizable deviations of the forward–backward observables at the ILC running above the Z mass and with longitudinally polarized electron and positron beams. The ability of the ILC to probe these models via high-precision measurements of the forward–backward asymmetry is discussed. Alternative scenarios at other energies and beam polarization schemes are also discussed, extrapolating the estimated uncertainties from the two baseline scenarios.

1 Introduction

The Standard Model (SM) is a successful theory, well-established experimentally and theoretically. With the discovery of the Higgs boson [1,2], the structure of the SM seems to be confirmed. However, the SM cannot explain many of its seemingly arbitrary features. An example is the striking mass hierarchy in the fermion sector. Moreover, while the dynamics of the SM gauge bosons, the photon,

H. Yamamoto: On leave from Tohoku University, Sendai, Japan.

[a] e-mail: adrian.irles@ific.uv.es (corresponding author)

W and Z bosons, and gluons are governed by the gauge principle, the dynamics of the Higgs boson are different and unique in the SM. The SM does not predict the strength of the Higgs couplings of quarks and leptons, nor the Higgs self-couplings. Large quantum corrections must be canceled by fine-tuning the parameters to match the measured Higgs boson mass. One possible solution to this issue, achieving stabilization of the Higgs mass against quantum corrections, appears when the Higgs boson is associated with the zeroth mode of a dimension-five component of extensions of the SM gauge group. These models are referred to as gauge-Higgs unification (GHU) models.

The two most precise determinations of $\sin^2 \theta_{\text{eff}}$ by the LEP and SLC differ by 3.7 standard deviations, and neither agrees with the SM prediction [3,4]. In particular, the LEP value was extracted from the forward–backward asymmetry measurement for b-quarks in LEP1 data, and is nearly three standard deviations away from the value predicted by the SM. Clarifying this anomaly and exploring the possibility of BSM physics motivates the study of quark pair production in high energy e^-e^+ collisions at future colliders both at the Z boson mass and higher energies. In the SM, these interactions are mediated by the photon, Z boson, and their interference. Some BSM theories predict deviations of these bosons' couplings or even sizable new contributions to these processes from new mediators (such as heavy Z' resonances). These deviations would be accessible experimentally by performing high precision measurements of $e^-e^+ \rightarrow q\bar{q}$ observables at different center-of-mass energies ($\sqrt{s}$). The work presented here is based on the study of such processes at the ILC.

In parallel to the exploitation of data from the Large Hadron Collider (LHC), the high-energy accelerator-based

particle physics community is working towards the next large colliders after the LHC. On one hand, there is the Electron-Ion Collider (EIC) which has been recently approved for construction at Brookhaven National Laboratory [5]. On the other hand, various projects of high-energy e^-e^+ colliders have been proposed and are under discussion. These "Higgs Factories" are designed for the precise scrutiny of the Higgs sector and search for new physics through precision measurements. We here discuss in detail the International Linear Collider (ILC) which we consider the most mature from a technological point of view, having produced a technical design report (TDR) in 2013 [6–10]. The ILC plans for a comprehensive high-precision physics program based on collisions of polarized electron and positron beams at a center-of-mass energy of 250 "ILC250" and 500 GeV "ILC500". Operation around the $t\bar{t}$ production threshold, the Z-mass, and at 1 TeV are also proposed. The studies discussed in this document are based on full simulations of the International Large Detector (ILD) concept [10,11]. The ILD is one of the detectors proposed for collecting and exploiting the ILC data. It has been optimized to perform high-precision measurements at ILC250 and ILC500.

Other proposals for Higgs factories, not discussed in this document, are the Compact Linear Collider (CLIC [12–14]), the Future Circular e^-e^+ Collider (FCCee [15,16]), the Circular electron-positron Collider (CEPC [17,18]) and the Cool Copper Collider (C^3 [19]). The CLIC and C^3 are linear colliders with baseline design collision energies of 380, 1000, and 3000 GeV (for CLIC) or 250 and 550 GeV (for C^3). Both foresee using longitudinal polarization only for the electron beam. The FCCee and CEPC are electron-positron circular colliders featuring only longitudinally unpolarized beams and with baseline collision energies at the Z mass and 240 GeV with an eventual upgrade to 365 GeV, at least for the FCCee case. Intermediate energy stages around the WW production threshold are also envisioned.

The content of this article is structured as follows. Section 2 briefly describes the two GHU models used as benchmarks and discusses the sensitivity of the forward–backward asymmetry, A_{FB}, in $e^-e^+ \rightarrow b\bar{b}$ and $e^-e^+ \rightarrow c\bar{c}$ processes at different energies and beam polarization scenarios. Section 3 describes the ILC, the ILD, and the experimental framework for the study presented here. Section 4 presents a detailed discussion of the methodology and prospects for precisely measuring A_{FB}^c and A_{FB}^b at ILC250 and ILC500, based on previous full simulation studies [20,21]. Section 5 discusses the potential of indirect constrains on the two aforementioned GHU theories through the measurement of A_{FB}. Conclusions and prospects are discussed in Sect. 6.

2 Theory

2.1 Gauge-Higgs Unification Models

The $SU(3)_c \times SO(5)_W \times U(1)_X$ GHU models on a Randall-Sundrum (RS) warped space have been studied as candidates to explain physics beyond the SM, where $SO(5)_W \times U(1)_X$ contains the electroweak gauge symmetry $SU(2)_L \times U(1)_Y$ [22–30]. In this scenario, the Higgs field naturally appears as a fluctuation mode of the Aharonov-Bohm phase θ_H in the extra dimension. Gauge symmetry stabilizes the Higgs boson mass against quantum corrections. With suitable parameter choices, low energy predictions of this gauge theory can match the SM. In this paper, two specific GHU models are considered: the A [25] and B [26] models. The only GHU models known so far that are consistent with the current experimental results are the A and B models based on the $SU(3)_c \times SO(5)_W \times U(1)_X$ symmetry.

Both models predict massive neutral vector bosons Z', which are the Kaluza-Klein (KK) modes of γ, Z, and Z_R (the $SU(2)_R$ gauge boson). Here, we simply describe the models and parameter sets that are used in this paper. For the full description see Refs. [22–30].

In the A model [25], quark-lepton multiplets are introduced in the vector representation of $SO(5)$. The non-observation of Z' at the LHC implies limits $\theta_H \lesssim 0.09$, $m_{KK} \gtrsim 9$ TeV [28]. Whether the coupling of the Z' bosons is stronger to right- or left-handed fermions depends strongly on the sign of the bulk mass of fermions. The couplings of the right-handed fermions to the Z' are large since positive bulk masses of fermions are chosen to avoid large deviations of the Z boson couplings to fermions. In this paper, two parameter sets of the A model (A_1 and A_2) are adopted as benchmark points [31][1]:

$A_1 : \theta_H = 0.0917, m_{KK} = 8.81$ TeV$\rightarrow m_{Z^1} = 7.19$ TeV;
$A_2 : \theta_H = 0.0737, m_{KK} = 10.3$ TeV$\rightarrow m_{Z^1} = 8.52$ TeV,
where Z^1 is the first KK Z boson. The masses of the first KK γ and Z_R bosons are similar to those of the first KK Z boson. The parameters are chosen such that the couplings of the SM-like Z boson to fermions (other than the top quark) agree with current measurements within one part in 10^4. The values of m_{KK} and θ_H for which the top quark and the Higgs boson masses and electroweak symmetry breaking can be realized are strongly restricted. The m_{KK} value in the parameter set A_2 is at the maximum reachable in the A model.

In the B model [26], which is inspired by grand unification, the quark-lepton multiplets are introduced in spinor, vector, and singlet representations of $SO(5)$. More specifically, this model is constructed as a low-energy effective description of the $SO(11)$ gauge-Higgs grand unification model on the RS

---

[1] The parameter sets A_1 and A_2 correspond to A_2 and A_3 in [31], respectively.

warped space [32,33], and the representations of $SU(3)_c$, $SO(5)_W$, and $U(1)_X$ that can be introduced are strongly restricted by $SO(11)$ gauge symmetry. The non-observation of Z' and W' signals at LHC implies limits $\theta_H \lesssim 0.10$, $m_{KK} \gtrsim 13$ TeV [28]. At the High-Luminosity LHC with an integrated luminosity of 3000 fb^{-1} and $\sqrt{s} = 14$ TeV, it may be possible to search up to $m_{KK} \simeq 22$ TeV for the GHU B model [28]. However, in the studies of Ref. [28], background processes are ignored, and the acceptances and efficiency are not taken into account. In this paper, six parameter sets of the B model, $B_j^{\pm}$ ($j = 1, 2, 3$), are adopted as benchmark points [29,30][2]:

$B_1^{\pm}$: $\theta_H = 0.10$, $m_{KK} = 13$ TeV $\rightarrow m_{Z^1} = 10.2$ TeV;
$B_2^{\pm}$: $\theta_H = 0.07$, $m_{KK} = 19$ TeV $\rightarrow m_{Z^1} = 14.9$ TeV;
$B_3^{\pm}$: $\theta_H = 0.05$, $m_{KK} = 25$ TeV $\rightarrow m_{Z^1} = 19.6$ TeV;

where the superscripts $\pm$ indicate the sign of the lepton bulk masses. The bulk masses of the quarks are negative in all parameter sets since very light vector-like quarks appear when the bulk masses of the quarks are taken to be positive. Model parameters are chosen such that Z couplings to fermions (other than the top quark) agree with the SM within one part in 10^3. These models make use of the so-called 4D bare Weinberg angle (a projection of the electroweak mixing angle), which is defined such that all the parameter sets in the B model predict values of A_{FB} ($e^- e^+ \rightarrow \mu^- \mu^+$) compatible with current best measurements [27]. For B_j^+, the coupling of right-handed electron to the Z' boson is larger than that of the left-handed electron; for B_j^-, the coupling of left-handed electron to Z' boson is larger than that of the right-handed electron.

2.2 Forward–backward asymmetry predictions in GHU

The forward–backward asymmetry, A_{FB}, is defined as

$$A_{FB}^q = \frac{\sigma^F - \sigma^B}{\sigma^F + \sigma^B}, \tag{1}$$

where $\sigma^{F/B}$ is the $e^- e^+ \rightarrow q\bar{q}$ cross-section in the forward (F) and backward (B) hemisphere as defined by the polar angle of the quark θ_q in the nominal center-of-mass reference frame and with respect to the electron beam direction. For each of the models described above, A_{FB} has been calculated at leading order for b and c-quark production in several $e^- e^+$ scenarios at various center-of-mass energies and beam polarizations. We use the (P_{e^-}, P_{e^+}) notation for beam polarization, in which the first term is for the electron and the second for the positron beam, a negative sign signifies a left-handed polarization, and 0 corresponds to un-polarized and ± 1 to fully polarized beams.

The deviations from the SM value of A_{FB} induced by the different models are shown in Fig. 1 at 250, 500, and 1000 GeV, with and without ILC-like beam polarization. The expected differences increase with energy and show large variations depending on the model and the beam polarization. At 250 GeV, the largest deviations occur in b-quark pair production with $(+0.8, -0.3)$ beam polarization, with the highest values for the A models. At 500 GeV, c-quark pair production also shows large deviations in $(+0.8, -0.3)$ for the A models and in $(-0.8, +0.3)$ for the B models. At 1 TeV, most models show sizeable deviations for at least one of the discussed channels.

3 Experimental framework

3.1 The international linear collider and the international large detector

The International Linear Collider (ILC) is a linear electron-positron collider that will produce collisions at several energies, and feature a high degree of longitudinal polarization for both beams. This article focuses on collisions at center-of-mass energies of 250 GeV and 500 GeV (ILC250 and ILC500) in the baseline running scenario, so-called H20-staged [34]. The H20-staged scenario assumes different integrated luminosities split between left-handed and/or right-handed electron and positron beams. In addition, we also briefly discuss other scenarios such as operation at the Z-pole (ILCGigaZ) and 1 TeV (ILC1000). This information is summarized in the Table 1.

The International Large Detector (ILD) is one of the detectors proposed for collecting and exploiting the ILC data. The ILD design is optimized for the reconstruction of final state particles using Particle Flow techniques [35,36]. ILD consists of inner vertexing and tracking systems and high granularity calorimeters within a 3.5 T solenoid, followed by an instrumented flux return used to identify muons. A detailed description of the different subsystems and the proposed technological solutions can be found in Refs. [10,11]. The tracking systems in the current ILD design are briefly discussed due to their crucial role in the studies presented in this paper.

The vertexing and tracking systems are based on silicon sensors and a time projection chamber (TPC). The vertex detector (VTX) is the closest to the beam pipe, spanning radii from 16 to 60 mm. Its design is optimized to provide a single hit resolution of 3 μm. The ILC bunch train structure allows for power-pulsed operation, reducing power consumption and cooling requirements by one to two orders of magnitude. Low-mass passive cooling technologies can therefore be used, resulting in a material budget of around
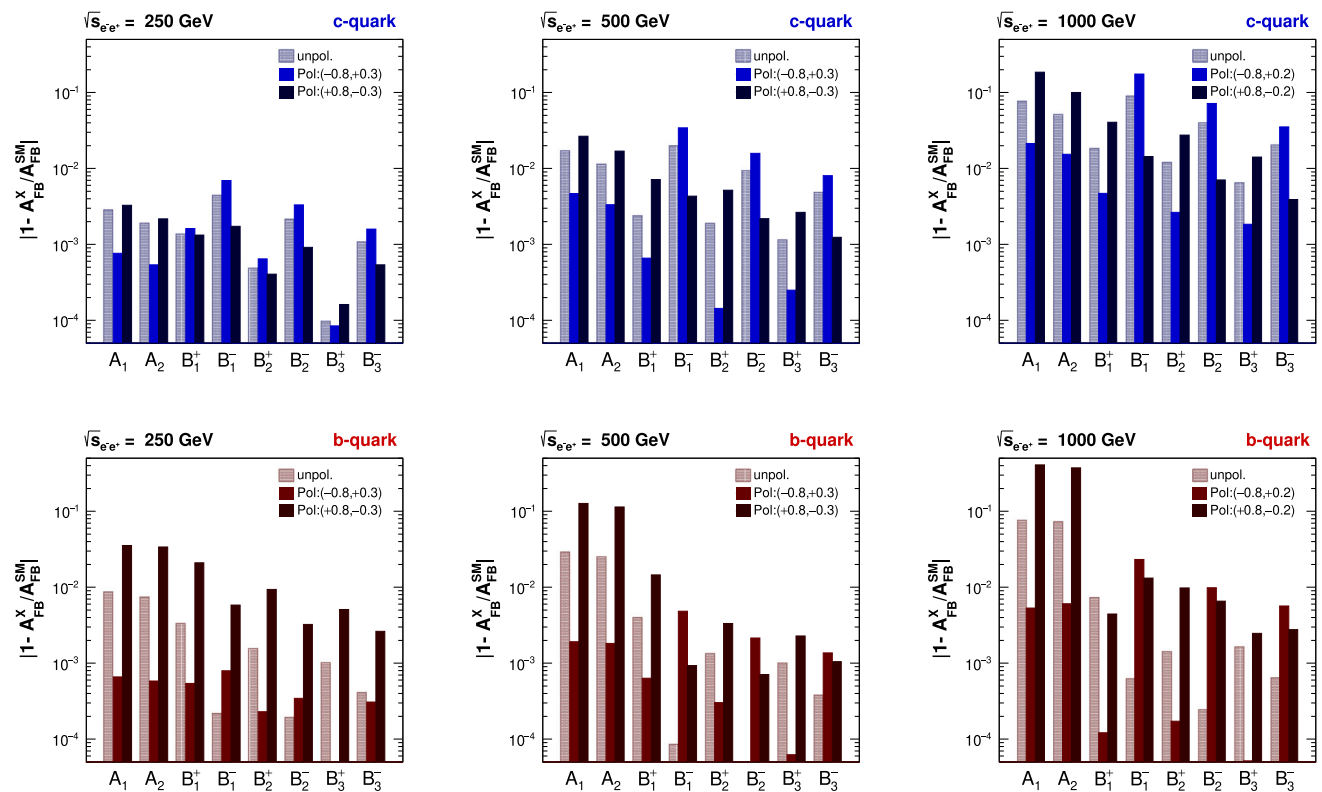
---

[2] The parameter sets $B_1^{\pm}$, $B_2^{\pm}$, and $B_3^{\pm}$ correspond to $A^{\pm}$, $B^{\pm}$, and $C^{\pm}$ in [29,30], respectively.

Fig. 1 Predicted differences for the A_{FB} observable in e^-e^+ collisions at several $\sqrt{s}$ between different GHU models and the SM. The expectations for different final states for c-quark or b-quark pair production and different longitudinal beam polarizations are compared for each energy

Table 1 Considered integrated luminosities, $\int \mathcal{L}$, and beam polarization degree scenarios considered in this work. The second row gives the degree of beam polarization for electrons and positrons. The third row shows the split of the total integrated luminosities when operating with opposite sign polarization (OSP) or same sign polarization (SSP) beams

	ILCGigaZ	ILC250	ILC500	ILC1000
$\int \mathcal{L}\,[fb^{-1}]$	100	2000	4000	8000
$(|P_{e^-}|, |P_{e^+}|)$	(0.8,0.3)	(0.8,0.3)	(0.8,0.3)	(0.8,0.2)
OSP|SSP [%]	40|10	45|5	40|10	40|10

0.15% of a radiation length per layer, thereby minimizing multiple scattering.

Silicon tracking systems follow the VTX detector: the silicon internal tracker (SIT) covers the central region, and the forward tracking detector (FTD) extends the coverage to lower angles closer to the beam axis. The SIT also features a barrel geometry and covers the region between 16° and 164° with respect to the beam axis. The FTD comprises disks perpendicular to the beam axis and is designed to cover the low-angle region down to 4.8°, complementing the SIT coverage between 16° and 32°. The TPC is a large volume time projection chamber allowing continuous 3D tracking and charged particle identification based on the specific energy loss dE/dx. It has a length of 4 m and spans radii from 329 to 1808 mm, providing up to 220 track measurements with a position resolution in the $r - \phi$ plane of around 100 µm

and a dE/dx resolution of approximately 4.5% with pad-based readout. An alternative approach read out by 55 µm pixels has the potential for improved performance. Simulations extrapolating beam test results show that an improved relative resolution of $\sim$ 3–4% will be feasible using cluster counting techniques (dN/dx) instead of the traditional dE/dx approach [37].

3.2 Event simulation

The results in this paper are based on full simulation samples of ILC250 and ILC500 provided by the ILD concept group. All simulations use the ILD-L [11] model, whose geometry, material, and readout are implemented in DD4HEP [38], interfaced with Geant4 [39–41]. Inactive materials describing cables, support structures, and services are accounted for

in the simulation and reconstruction. SM signal and background events are generated with the WHIZARD v2.8.5 [42] event generator at LO, including QED ISR in perturbative leading-logarithmic approximation. Parton shower and hadronization effects are simulated by the Pythia 6.4 event generator [43]. The beam energy spectrum and beam-beam interaction producing incoherent e^-e^+ background pairs are generated with Guinea-Pig [44]. Other background sources, such as $\gamma\gamma$ to low p_T hadrons, are generated separately and overlaid on the simulated events [45]. A description of the whole procedure to generate all SM processes is given in [46]. Each set of samples features fully longitudinally polarized beams in various configurations. Samples with realistic polarization scenarios are obtained by merging these samples with appropriate weights.

This work is based on the analysis of $e^-e^+ \to q\bar{q}$ events at high center-of-mass energies [20,21]. In the SM, at $\sqrt{s}$ larger than the Z boson mass, these processes are sensitive to γ and Z-couplings. However, due to QED ISR, the center-of-mass energy of the e^-e^+ system may be reduced with respect to the $\sqrt{s}$ of the collider. Furthermore, if the energy radiated in the QED ISR process is large enough, the e^-e^+ system may undergo a radiative return to the Z-pole, producing an on-shell $Z \to q\bar{q}$ process.

The ISR changes the kinematic event properties, so such events can be distinguished from the high mass signal events. It is therefore treated as a background, which we name "$\gamma q\bar{q}$" or "radiative-return". For a formal separation between the signal and radiative-return processes, we define as signal those events with a quark-pair invariant mass larger than 140 GeV for ILC250 (200 GeV for ILC500) and acolinearity smaller than 0.3, with acolinearity defined as in Eq. 7 from [20], using a simplified definition of the acolinearity

$$\sin \Psi_{acol} = \frac{|\vec{p}_q \times \vec{p}_{\bar{q}}|}{|\vec{p}_q| \cdot |\vec{p}_{\bar{q}}|}, \tag{2}$$

with $\cos \Psi_{acol} < 0$.

Other sources of backgrounds are due to hadronically decaying di-boson or, for ILC500, top-quark pair production. The cross sections for all these processes, involving $q = u, d, s, c, b$ in the final state, are summarized in Table 2.

3.3 Event reconstruction

The ILD track reconstruction [11,47] is based on pattern recognition algorithms carried out independently in the different parts of the tracker systems. This is followed by the combination of all the track candidates and segments for a final refit performed with a Kalman filter. The entire process is implemented in the MarlinTrk framework, which is part of the ILCSoft toolkit. The resulting tracks are combined with calorimeter hits in the Pandora particle flow algorithm

(PFA) [48] to produce a set of particle flow objects (PFO), each of which should correspond to a final-state particle.

3.3.1 Vertex and jet reconstruction

Once the PFOs are reconstructed, vertex reconstruction, jet reconstruction, and jet flavor tagging are performed using LCFIPlus [49]. The primary vertex of the event is found in a tear-down procedure, starting with all tracks and gradually removing tracks less compatible with being associated with the primary vertex hypothesis. In a second step, LCFIPlus performs an iterative reconstruction of secondary vertices. Jets are reconstructed using the VLC algorithm [50] for e^-e^+ colliders in exclusive two-jet mode. This algorithm includes additional beam jets which are disregarded.

3.3.2 Flavor tagging

The b and c-quark tagging are performed by LCFIPlus using boosted decision trees (BDTs) based on sensitive variables from tracks, vertices, and charged-hadron identification using TPC information. BDTs are trained using reconstructed jets in $e^-e^+ \to q\bar{q}$ events at $\sqrt{s} = 250$ or 500 GeV accordingly [21]. Particle Swarm Optimization [51] with combined Kolmogorov–Smirnoff [52–54] and Anderson–Darling [55–57] tests are applied to optimize the BDTs performance while avoiding overtraining. The resulting BDT working points are chosen to limit the mistagging of the other quarks to $\sim 1.5\%$ ($\sim 3\%$) in the case of b-quark (c-quark) tagging.

3.3.3 Jet-charge measurement

The measurement of the differential cross-sections and A_{FB} requires measuring the jet charges, i.e. the separation of jets originating from quarks and anti-quarks. Two methods are used to measure the jet-charge [20]: the *Vertex Charge* and *Kaon Charge*.

Vertex charge, Vtx-method

The Vertex Charge is defined as the sum of the charges of all tracks associated with reconstructed displaced vertices within a jet. The perfect application of the method requires that all charged tracks from b or c-hadron decays are correctly measured and associated with the jet's secondary vertex.

The tracking efficiency in ILD for isolated tracks with momentum above 1 GeV, transverse momentum above 100 MeV and $|\cos \theta| < 0.85$ is estimated to be close to 100% and better than 99% in the very forward direction [11]. However, when reconstructing secondary vertices in dense jets, loss of tracks or incorrect association with secondary vertices may not be negligible. It has been estimated that up to $\sim 5\%$ of the tracks may be missed during vertex reconstruction, espe-

Table 2 Expected cross sections for signal ($q\bar{q}$) and main background processes

Process	ILC250		ILC500	
σ [pb]	$(-0.8, +0.3)$	$(+0.8, -0.3)$	$(-0.8, +0.3)$	$(+0.8, -0.3)$
$q\bar{q}$	17.2	6.4	2.9	2.0
$\gamma q\bar{q}$	60.2	39.3	16.3	9.5
$q\bar{q}q\bar{q}$ (no Higgs)	16.2	1.5	8.2	0.6
$HZ \to q\bar{q}H$	0.2	0.1	0.07	0.05
$b\bar{b}q_1\bar{q}_2q_3\bar{q}_4$	–	–	0.4	0.2

cially in the very forward and backward regions [20]. This is particularly relevant for b-quark jets due to the large number of secondary tracks per jet: most jets have between two and five (and in rare cases up to fifteen) displaced tracks. In contrast, most c-quark jets contain two displaced tracks. The difference in performance for the two flavors can be qualified by P_{chg}, the probability that the jet charge reproduces the sign of the charge of the initial quark.

Kaon charge, K-method

The charge of the jet can also be estimated by the charge sum of all kaons associated to displaced vertices inside the jet. These kaons are produced in decays of D-mesons and B-hadrons. The performance of this method is limited mostly by charged-kaon identification capabilities and physics processes such as $B^0 - \bar{B}^0$ oscillations. The baseline ILD design foresees a $K^\pm/\pi^\pm$ separation power of ~ 3[3] but an improvement is expected when using alternative TPC designs with larger pixelation allowing cluster-counting reconstruction, dN/dx, in place of the traditional dE/dx [37]. We implemented this feature of improved reconstruction in our analysis, such that the TPC track reconstruction offers $K^\pm/\pi^\pm$ separation power up to 4 using dN/dx measurements for tracks with momentum between $\sim (3-30)$ GeV. A detailed description of the discriminating variables and procedure can be found in [21] where it is shown that using dE/dx for single charged-kaon identification in displaced tracks inside jets, we can get up to an $\sim 80\%$ efficiency with $\sim 80\%$ purity for the $b\bar{b}$ case at ILC250 and ILC500, an $\sim 80\%$ efficiency with $\sim 90\%$ purity for the $c\bar{c}$ case at ILC250 and an $\sim 80\%$ efficiency with $\sim 80\%$ purity for the $c\bar{c}$ case at ILC500 (because of the higher momentum of displaced tracks compared with ILC250). However, for the dN/dx at the ILC250 scenario, we can work at the points with 90% efficiency and $\leq 95\%$ for both final states. At ILC500, the purity is slightly worse due to the higher momentum of the displaced tracks but still above the 90%.

---

[3] The separation power is calculated as defined in Eq. 8.3 of Ref. [11]

3.3.4 Event preselection

Once events are reconstructed, a preselection is based on a series of kinematic cuts applied to enrich the data sample of $q\bar{q}$ ($q = u, d, s, c, b$) signal events, expected to show back-to-back two-jet kinematics, while removing the backgrounds. The largest background contamination is the radiative-return background associated with QED ISR. Most QED ISR will be collinear to the beam and, if energetic enough, will result in a reconstructed invariant mass of the two-jet system significantly smaller than $\sqrt{s}$, making it straightforward to filter such events. However, a non-negligible fraction of the radiative-return events, $\sim 10\%$ according to the existing simulations, will radiate photons inside the detector volume, requiring other kinematic variables, defined in the following, to be used to filter these events.

We define two new objects, $\gamma_{clus,j}$, by clustering all uncharged PFOs within each jet (j). We denote the most energetic of these two as $\gamma_{clus.}$. The reconstructed energy and angles of $\gamma_{clus.}$ will be used for the event selection. Another variable used is y_{23}, the distance (as defined by the VLC algorithm) at which the event transitions from a two to a three-jet topology. We also use the invariant mass of the two-jet system (m_{jj}). The selection requirements for ILC250 are summarized in the following, with the modifications for ILC500 shown inside parentheses:

1. photon veto cuts, rejecting events if:

   (a) at least one of the jets contains only one PFO;
   (b) if the energy of $\gamma_{clus.}$ is larger than 115 GeV (220 GeV) or it is reconstructed in the forward region $|\cos\theta| > 0.97$;

2. events with $(\sin\Psi_{acol})_{jj} > 0.3$ are rejected;
3. events with $m_{jj} < 140$ GeV (200 GeV) are rejected;
4. events with $y_{23} > 0.02$ (0.007) are rejected.

Cuts 1 to 3 are designed to reduce the contamination from the radiative-return backgrounds, and cut 4 is most effective against di-boson backgrounds. The last cut is significantly tightened at ILC500 to reduce the much larger WW background contamination in the case of left-handed elec-

tron beam polarization. This cut reduces the efficiency from $\sim 75\%$ to $\sim 55\%$ while keeping the background over signal B/S ratio below $3 - 5\%$. At ILC500, cut 2 (on acolinearity) reduces the $t\bar{t}$ contribution to the 1% B/S level, and cut 4 further reduces the $t\bar{t}$ background to negligible levels.

The event selection has been thoroughly studied and documented in Refs. [20,21]. According to these studies and the references cited, a constant within the percent-level or less high-efficiency rate is obtained in the entire detector volume, except for the very forward/backward region of $|\cos\theta| > 0.9$, where the efficiency rapidly drops. This drop in efficiency is due to the removal of events with high-energy photon candidates in that region in order to eliminate radiative-return events, as well as the decrease in tracking and vertexing performance, which impacts the flavor tagging algorithms. In Ref. [20], it was cross-checked that, within current uncertainties and using leading-order simulations, the difference between extrapolating over or ignoring that region is negligible and does not affect the analysis. In the present analysis, we have followed the former alternative. However, we emphasize the importance of the optimization of detector layout and reconstruction tools, especially in the forward/backward region. This is currently being discussed within the ILC Concept Group as well as within the Higgs Factory detector concepts [11,58–60].

4 Experimental reconstruction of the forward–backward observable using full simulation tools at ILC250 and ILC500

This section describes the most critical aspects of the experimental reconstruction of the observable forward–backward asymmetry A_{FB}^q by measuring $\frac{d\sigma}{d\cos\theta}$. This work is based on a previous ILD study [20,21]. The method starts with a preselection that results in a highly pure $q\bar{q}$ sample, followed by the double flavor tagging (Sect. 4.1) which selects b-quark (or c-quark) events, and ends with the double charge (Sect. 4.2) measurement to distinguish between quark and anti-quark jets. The differential cross-section is extracted from the measurement of the total number of events reconstructed as a function of the quark-jet scattering angle θ:

$$\frac{dN}{d\cos\theta} = \mathcal{L}\left[\varepsilon_{pre}\varepsilon_{DTC}\frac{d\sigma}{d\cos\theta} + \varepsilon_{bkg}\frac{d\sigma_{bkg}}{d\cos\theta}\right] \quad (3)$$

where $\mathcal{L}$ is the integrated luminosity and the ε variables are the different selection efficiencies, defined as a function of $|\cos\theta|$. The signal preselection efficiency (ε_{pre}) and the background selection efficiency (ε_{bkg}) are estimated using only Monte Carlo data.

4.1 Double tagging method

The Double Tag method (DT) [3] is based on the comparison of single and double flavor-tagged samples for the simultaneous extraction of the tagging efficiency, ϵ_q and the hadronic cross-section fraction R_q.[4] The method is applied once we have preselected an enriched $q\bar{q}$ sample reconstructed as two jets. We next apply flavor tagging to all jets, and extract two numbers: the fraction of all jets tagged as being of flavor q, and the fraction of events in which both jets are tagged as flavor q. The exact formulation is described in Ref. [20] for a fully differential analysis, in contrast to the integral analyses performed in the past. By comparing these two ratios for b-quark and c-quark, we can simultaneously measure the efficiency of the flavor tagging algorithm (ϵ_q) and R_q for both flavors.

Although the method is based on data comparisons, some initial hypotheses, based on simulations, are required. For instance, it is assumed to be an almost background-free analysis (or to have a perfectly modeled background). This was easier to achieve at LEP and SLC running at the Z-pole. For data taken in the continuum above the Z-pole, a tighter preselection is required to minimize the background contribution of the radiative return or di-boson hadronic decays. The method also assumes knowledge of the mis-tagging efficiencies, the probability of tagging a true q' as q. The size of these mis-tagging efficiencies and their uncertainties will directly impact the uncertainty of the measurements. This factor was one of the dominant sources of uncertainty for the measurements at LEP and SLC, with less relevance in the latter case due to its improved flavor-tagging capabilities (especially for the c-quark). Finally, the method assumes that the quark-tagging efficiencies are symmetric between the two sides of the detector (positive and negative $\cos\theta$). However, effects such as the resolution on the primary vertex reconstruction, inhomogeneities in the detector layout or performance, or kinematic variations of the back-to-back topology due to hard gluon radiation may introduce correlations. These correlations can be parametrized by ($1+\rho_q$), known in the literature as the hemisphere or jet angular correlation. With this notation, the double-tag efficiency is given by $\epsilon_q^2 \cdot (1 + \rho_q)$. This parameter is the only one that is calculable only using Monte Carlo simulations, and it was considered a significant source of uncertainty in past experiments. It was less of an issue at SLC than at LEP thanks to the more precise primary vertex determination. The jet angular correlation is expected

---

[4] The hadronic cross-section fraction is defined as

$$R_q = \frac{\sigma_{e^-e^+\to q\bar{q}}}{\sigma_{had.}} \quad (4)$$

where $\sigma_{had.}$ is defined as $\sigma_{e^-e^+\to q\bar{q}}$ integrated over all quark flavors except the top-quark.

to be negligible in the case of the ILD at ILC [20] except in the forward detector region, where the tagging efficiency drops due to limited acceptance. In a fully differential analysis, these regions and others affected by detector issues can be removed from the study when performing a fit and be substituted by extrapolations (Table 3).

The preselection and DT selection efficiencies for the two flavors are shown in Table 4 for the ILC250 and ILC500.

4.2 Double charge method

The Double Charge method (DC) requires a pure $q\bar{q}$ sample (with q being only one flavor, c or b) for its application. It consists of the measurement of the charge of each jet using one of the methods described in Sect. 3.3.3. Only events with two oppositely charged jets are accepted. The experimental determination of the probability P_{chg} that the jet charge reproduces the sign of the charge of the quark of the hard scattering is straightforward [20]. Since the Vtx-method and the K-method show similar values of P_{chg}, it is also possible to use mixed cases in which opposite jets use different methods. In Ref. [20], three different categories are defined and studied for each flavor:

1. The charge of both jets has been measured with the method that more often gives a non-zero charge measurement (primary method).
2. Only one jet has no measurement of its charge with the primary method but does have it with the other method (secondary method).
3. Both jets have their charge measured with the secondary method.

For the b-quark, the primary method is the Vtx-method, while for the c-quark case it is the K-method. The algorithm defined in Ref. [20] has the benefit that it does not rely on the determination of the efficiency of each method since it only uses the measured fractions, f, of jets with non-zero charge measurements and the probability of having correctly measured the sign of the charge. For the latter, we use the P_{chg}, first introduced in Sect. 3.3.3, measured using the data sample itself by comparing events with the same sign of the charge measurements for both jets and events with different signs. With simple combinatorics calculations, the experimental P_{chg} values will be extracted without the need for Monte Carlo simulations. This procedure is performed differentially, in small bins of $\cos\theta$.

The DC measurements minimize the migrations between hemispheres due to wrongly measured jet charge. However, these migrations are not negligible in the b-quark with high left-handed electron-beam polarization case, even using the DC. The reason is twofold: the relatively small P_{chg} for the b-quark case (as explained in Sect. 3.3.3) and the large value

of A_{FB} that produces a larger amount of event migration from the forward to the backward region than from backward to forward. This has a sizable impact on the reconstructed differential distribution, with localized deviations of the differential cross-section of up to a factor of three in the region $\cos\theta \lesssim -0.75$. These migrations can be easily corrected using the measured values of P_{chg}, which give the probability that the charge has been wrongly measured in both jets, hence flipping the sign of $\cos\theta$ [20].

The efficiency of the full selection, including preselection, DT, and DC selection for the two flavors, are shown in Table 4 for the ILC250 and ILC500 cases, for the full detector volume, i.e., including the forward regions.

4.3 Estimation of A_{FB}

Once the DT and DC methods have been applied, all the inputs needed to extract the efficiency of double tagging and charge measurement, ε_{DTC}, and to infer $d\sigma/d\cos\theta$ are available. The efficiency is estimated for every flavor and each DC category, and the statistical uncertainties are propagated accordingly [20]. The correction for the efficiencies is performed differentially as a function of $|\cos\theta|$.

The result of the entire correction procedure is shown in Fig. 2 for the different flavors and running scenarios using SM samples.

For the estimation of A_{FB}, the function

$$\frac{d\sigma}{d\cos\theta} = S\left(1 + \cos^2\theta\right) + A\cos\theta \tag{5}$$

is fit to the reconstructed distributions. Note that this function neglects the SM tensorial contribution $T \times \sin^2\theta$, which is very small given the large boost of b and c-quarks. The fit is performed in the range of $|\cos\theta| < 0.9$, avoiding the very forward regions in which the acceptance decreases. The A_{FB} is extracted by extrapolating the fitted function to the full range of $\cos\theta$, and the statistical uncertainty is estimated for the expected integrated luminosity, including the uncertainties of the correction methods. The expected statistical uncertainties for the various running scenarios are shown in Fig. 3.

4.4 Systematic uncertainties

At ILC250 and ILC500, the expected statistical uncertainties on A_{FB} are at the level of a few per mil. A comprehensive study of the leading experimental systematic uncertainties is reported in Ref. [20]. The most significant systematic uncertainties on A_{FB} are due to the preselection efficiency, the hadronization/fragmentation modeling, the angular correlations due to QCD effects, and the knowledge of the beam polarization. These are reported in the following. However,

Table 3 Jet charge performance of the different methods showing the fraction, f, of jets with non-zero charge measured by each method and the probability of having correct measurement, P_{chg}, as described in the text and in Ref. [20]. For simplicity, the values are given only for events excluding the forward regions $|\cos\theta < 0.9|$

	ILC250		ILC500	
	c [%]	b [%]	c [%]	b [%]
f_{Vtx}	36	65	49	75
f_K	49	48	51	72
$P_{chg,Vtx}$	93	83	92	82
$P_{chg,K}$	95	75	80	70

Table 4 Efficiencies and B/S estimated using ILD full simulation and reconstruction

	Eff(B/S)[%]			
	ILC250($-0.8, +0.3$)		ILC250($+0.8, -0.3$)	
Preselection:	$udscb$: 75.8(5.6)		$udscb$: 75.9(4.8)	
+DT	c : 9.5(0.6)	b : 38.1(0.9)	c : 9.4(0.5)	b : 38.1(1.3)
+DC	c : 3.7(0.5)	b : 14.7(0.8)	c : 3.7(0.5)	b : 14.7(1.2)
	ILC500($-0.8, +0.3$)		ILC500($+0.8, -0.3$)	
Preselection:	$udscb$: 54.4(7.4)		$udscb$: 54.5(5.0)	
+DT	c : 10.9(0.3)	b : 29.7(0.3)	c : 10.8(0.3)	b : 29.5(0.3)
+DC	c : 3.2(0.3)	b : 12.1(0.3)	c : 3.1(0.5)	b : 12.1(1.3)

we emphasize that the expected size of these systematic uncertainties is negligible compared to the statistical uncertainties expected at ILC when running above the Z-pole.

4.4.1 Pre-selection efficiency

Although this efficiency cancels in the numerator and denominator of the integral calculation of A_{FB}, the preselection efficiency cannot be neglected in a full differential analysis since it affects the shape of the differential measurement. The impact of this uncertainty has been evaluated by producing pseudo-data distributions applying uncorrelated 10% relative variations in bin-by-bin preselection efficiencies. This uncertainty is propagated to A_{FB}, giving rise to a relative uncertainty on A_{FB} of $\leq 0.1\%$. Uncertainties from background mis-modeling become mostly negligible, $\simeq 0.01\%$, due to the very efficient background rejection.

4.4.2 Hadronization/fragmentation modeling

Uncertainties on A_{FB} related to fragmentation are expected to be negligible thanks to the DT and DC methods. These were proposed and used by LEP and SLC experiments. These methods rely on the data for the estimation of the flavor tagging efficiencies, minimizing the usage of Monte Carlo tools for the modeling. Hence, fragmentation model uncertainties will only affect to the mis-tagging efficiency estimation but not the tagging efficiency. Furthermore, the mis-tagging rates will be much lower than at past experiments thanks to the high performance expected for modern flavor-tagging algorithms using modern statistical and machine-learning techniques and the progress in detector technologies.

4.4.3 Angular correlations

Full simulation studies suggest that the value of ρ_q at ILC250 is smaller than 0.2% throughout most of the detector volume [20]. The tracking system in the ILD simulation is symmetric, and no coherent noise is simulated, indicating that a non-zero ρ_q value can only be the result of occasional mis-measurements of the primary vertex or hard QCD radiation diluting the back-to-back configuration of the di-jet system. The small value of ρ_q suggests that both effects can be effectively controlled. This results from the small beam size (jet angular correlations due to a misplaced common vertex are suppressed) and an excellent tracking system. Moreover, a high tagging efficiency can significantly reduce jet angular correlations. To consider the impact of angular correlations due to QCD radiation, we assume they contribute an uncertainty of $\lesssim 0.1\% \cdot A_{FB}$, following Ref. [61], after having introduced acolinearity cuts in our definition of the signal and selection procedure. A full assessment of this effect would require simulations based on NLO QCD.

4.4.4 Beam polarization

Beam polarization uncertainties [62] influence the accuracy of precision measurements. For the measurement of A_{FB},
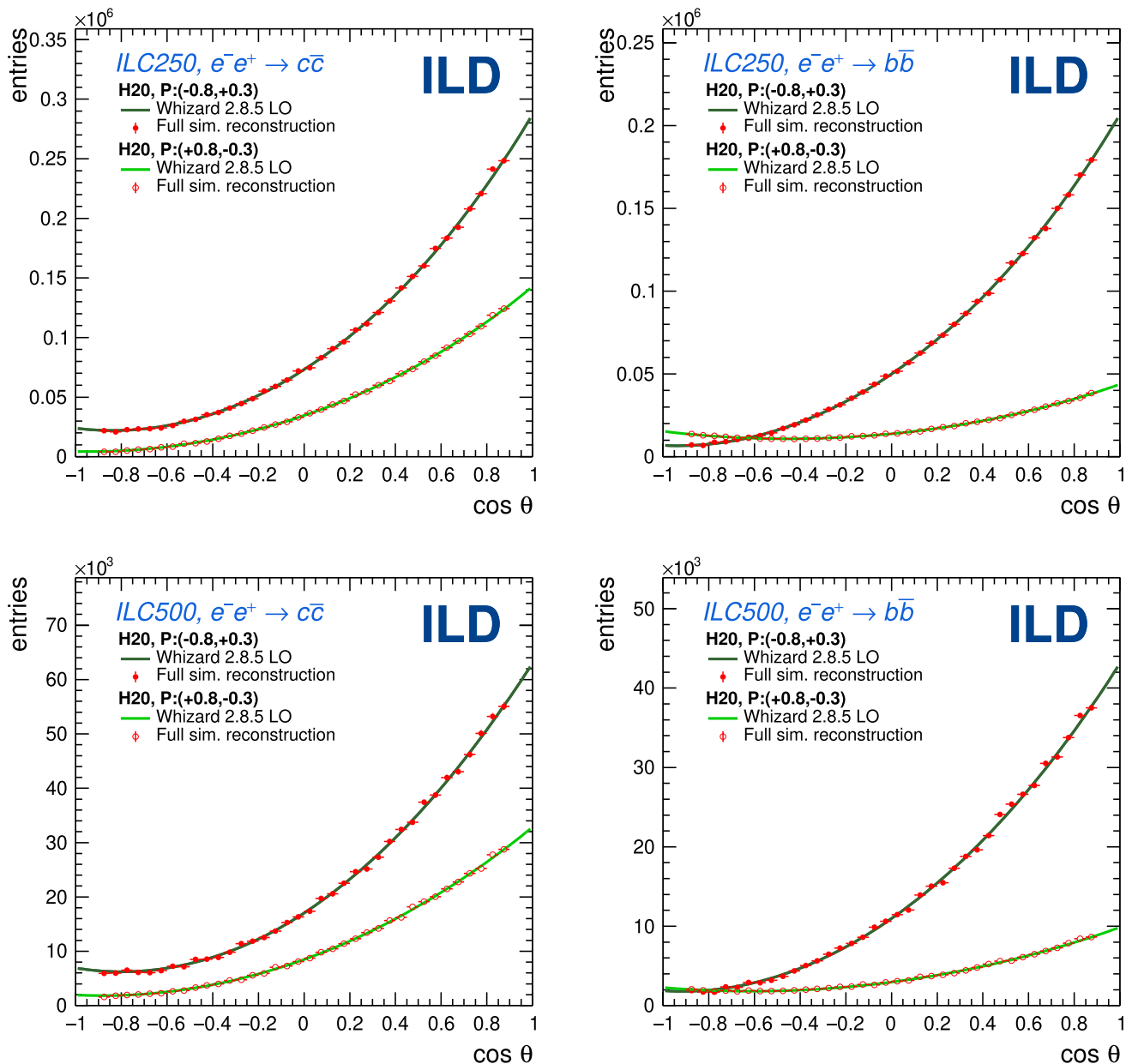
Fig. 2 Comparison of parton level and fully reconstructed $d\sigma/d\cos\theta$ distributions for different ILC scenarios and the b and c-quark

this uncertainty affects the b-quark and c-quark flavors differently, and has a non-negligible impact only on the right polarization scenario for the b-quark; in this scenario, we expect an uncertainty contribution of $0.15\% \cdot A_{FB}$ at ILC250, and somewhat smaller at ILC500 [20].

5 Statistical discrimination power for GHU models at ILC

The detailed studies described in the previous section result in a realistic estimation of the uncertainties on A_{FB} for the

b and c-quark at ILC250 and ILC500, with existing detector models and reconstruction tools. We have shown that the statistical uncertainties on A_{FB} expected at ILC running above the Z-pole are much larger than any systematic effects, which are therefore ignored in this section. Furthermore, we assume Gaussian uncertainties and uncorrelated measurements. This second approximation is motivated by the nature of the analysis, in which the DT and DC methods lead to the selection of fully independent samples for the different flavors and beam polarizations. Statistically independent MC simulations have been used to analyze the various polarization scenarios.
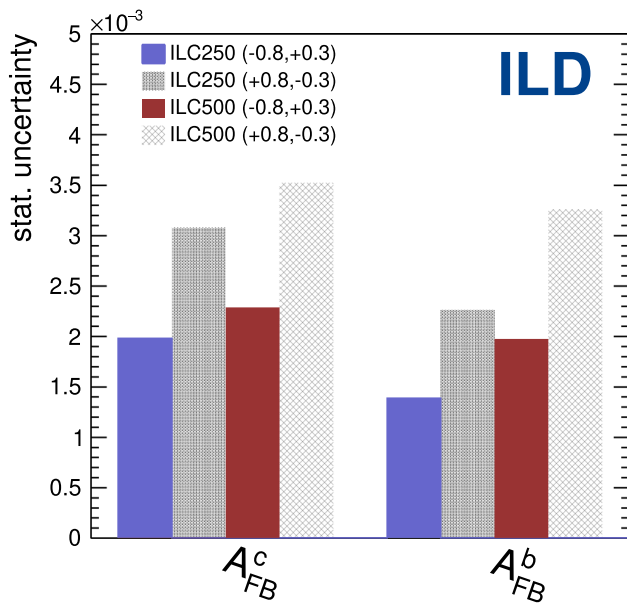
Fig. 3 Estimated statistical uncertainties on A_{FB}^c and A_{FB}^b using ILD full simulation and reconstruction at ILC250 and ILC500

To probe the potential of ILC to indirectly search for new physics, the significance when comparing two models, i and j, is defined as

$$d_{ij} = \frac{|A_{FB,i} - A_{FB,j}|}{\Delta A_{FB,j}} \tag{6}$$

with $A_{FB,i/j}$ being the A_{FB} predicted at leading order by model i or j, as explained in Sect. 2. The $\Delta A_{FB,j}$ corresponds to the expected statistical uncertainty of the forward–backward measurement at ILC, obtained as explained in Sect. 4. In addition, the systematic uncertainties arising from the limited knowledge of the exact value of the couplings in the SM prediction are added in quadrature to $\Delta A_{FB,j}$. For these estimates, we used different assumptions on the uncertainties on the Z-boson couplings to fermions and propagated them to the leading order calculation of A_{FB}. The different assumptions on these uncertainties extracted from Refs. [63,64] are:
C: current uncertainties, from LEP and SLC measurements;
R: expected uncertainties from measurements of radiative return events at ILC250;
Z: expected uncertainties from measurements at a dedicated ILCGigaZ run.

The probability for each $d \geq d_{ij}$ case and the discovery power discrimination are calculated in terms of the number of standard deviations from the null hypothesis for the model i. This is performed for each measurement and combined following the multivariate Gaussian formalism.

Figure 4 shows the expected discrimination power between the different GHU models and the SM for the different ILC running stages above the Z-pole foreseen by the H20-staged plan, ILC250 and ILC500. We have included two extra cases:

– ILC250$^\blacklozenge$ (*no pol.*): a hypothetical case of an ILC250 operating with un-polarized beams and assuming a total integrated luminosity equal to the baseline ILC250 scenario (2000 fb^{-1}). The ($\blacklozenge$) symbol is used to distinguish this case from the other studies, which use the nominal ILC beam polarization. This scenario can be compared with current circular collider proposals. Still, one should bear in mind that the simulated beam conditions are those of ILC and that the simulated ILD model has been optimized for the full range of ILC energies. Dedicated studies with full simulation of the beam conditions and detector models designed for circular colliders would be required to extract more definitive conclusions.
– ILC1000*: we have extrapolated statistical uncertainties from ILC500 to 8000 fb^{-1} at ILC1000, split according to the different polarization conditions as described in Table 1. The (*) symbol is used to distinguish this case from the three other cases, which use full simulation samples and reconstruction. At ILC1000, compared with ILC250 and ILC500, the experimental challenges are expected to be slightly different, with much more collimated jets and vertices and the possible presence of new backgrounds. However, no significant differences are expected in overall detector performance since the ILD has already been optimized to operate at ILC1000 (see [10,64] and references therein).

5.1 Requirements on the precision of the Z-fermion couplings measurements

Even if large deviations in the A_{FB} observables are measured at ILC250 or at higher energy in $e^- e^+ \rightarrow q\bar{q}$, one could still be unable to distinguish the contribution of new resonances from deviations from the SM Z-boson couplings. For this reason, high-precision measurements of the fermionic Z couplings are required. An ILCGigaZ run would allow the precise determination of all Z-boson couplings to fermions (except the top quark). Full simulation experimental studies are yet to be performed at the ILC and other Higgs Factories. First studies [64,65] show that an improvement of up to two orders of magnitude (including systematic uncertainties) could be obtained at the ILC for these couplings compared with the LEP and SLC. These studies include discussions of the most significant systematic uncertainties, which are expected to be 2–10 times larger than the statistical ones. Moreover, studies presented in Ref. [64] suggest that even at ILC250, such couplings could be measured with about
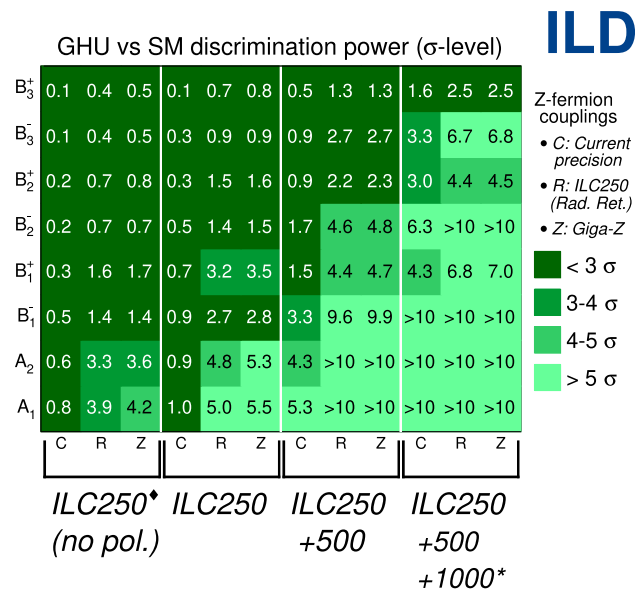
GHU vs SM discrimination power (σ-level)

ILD

	ILC250♦ (no pol.)			ILC250			ILC250 +500			ILC250 +500 +1000*		
	C	R	Z	C	R	Z	C	R	Z	C	R	Z
B_3^+	0.1	0.4	0.5	0.1	0.7	0.8	0.5	1.3	1.3	1.6	2.5	2.5
B_3^-	0.1	0.4	0.5	0.3	0.9	0.9	0.9	2.7	2.7	3.3	6.7	6.8
B_2^+	0.2	0.7	0.8	0.3	1.5	1.6	0.9	2.2	2.3	3.0	4.4	4.5
B_2^-	0.2	0.7	0.7	0.5	1.4	1.5	1.7	4.6	4.8	6.3	>10	>10
B_1^+	0.3	1.6	1.7	0.7	3.2	3.5	1.5	4.4	4.7	4.3	6.8	7.0
B_1^-	0.5	1.4	1.4	0.9	2.7	2.8	3.3	9.6	9.9	>10	>10	>10
A_2	0.6	3.3	3.6	0.9	4.8	5.3	4.3	>10	>10	>10	>10	>10
A_1	0.8	3.9	4.2	1.0	5.0	5.5	5.3	>10	>10	>10	>10	>10

Z-fermion couplings
- *C: Current precision*
- *R: ILC250 (Rad. Ret.)*
- *Z: Giga-Z*

< 3 σ
3-4 σ
4-5 σ
> 5 σ

Fig. 4 Statistical discrimination power between the GHU models described in the text and in [27,29,31] and the SM. Different running scenarios of ILC are compared: ILC250♦ (*no pol.*) (hypothetical case with no beam polarization and 2000 fb^{-1} of integrated luminosity), ILC250 (2000 fb^{-1}), ILC500 (4000 fb^{-1}), and ILC1000* (8000 fb^{-1}, not using full simulation studies but extrapolations of uncertainties from ILC500). Three different assumptions for the Z-fermion couplings uncertainties are considered [64]: C for current knowledge; R for expected knowledge after the full ILC250 program and the study of Z-fermion couplings from radiative return events, and Z for expected knowledge after a full ILCGigaZ program

one order of magnitude higher precision than at LEP/SLC by studying the radiative return to the Z-pole.

The impact of assuming improved precision on these couplings, according to the scenarios explained above, is shown in Fig. 4 in the different columns C, R, and Z. It shows that at ILC250, the precision on the Z couplings from a study of radiative return events allows one to approach the five standard deviations (σ) level for the discrimination of A models vs SM and get almost 3σ for the $B_1^\pm$. With ILCGigaZ precision, the discrimination power would be enhanced, allowing full discrimination of the A models. When including the higher energy stages of ILC, the difference between the two possible scenarios for improved Z coupling precisions becomes less critical due to the larger size of the new resonance contributions.

5.2 Importance of beam polarization and high energy reach

The ILC offers high-energy beams with a high degree of longitudinal polarization. This provides direct access to the different helicity amplitudes at different energies. This is particularly important for models predicting deviations in the right-handed electroweak couplings, which are less constrained by existing measurements. The comparison between

the first columns of Fig. 4, shows that the high degree of electron and positron beam-polarization at ILC250 offers a gain comparable to a factor two in integrated luminosity with respect to ILC250♦ (*no pol.*). Figure 1 shows that most of the sensitivity at ILC250 comes from the configuration with right-handed electron beam and left-handed positron polarization. An increase of statistics of this run from 900 fb^{-1} to ∼ 2.5 × 900 fb^{-1} would provide 5σ discrimination power for the A_1, A_2 and the $B_1^\pm$ GHU models (predicting $m_{KK} = 8.81$, 10.3 and 13 TeV respectively).

The production of an intense electron beam with a high degree of polarization is expected to be technically possible, while the positron source poses some technological challenges. To face these challenges, two options are being considered [64,66]. The baseline undulator-based positron source allows the production of polarized positron beams, while the other electron-driven concept would provide unpolarized positron beams. The baseline option provides 30% positron beam polarization at ILC250 and ILC500 and 20% at ILC1000. An upgrade could increase the polarization to 60%. We perform the exercise of comparing several scenarios for the positron beam polarization. The result is shown in Fig. 5 where we compare the discrimination power assuming three positron beam polarization scenarios: 0%, 30% and 60%,[5] all of them using extrapolated uncertainties from the R scenario for Z-fermion couplings. This figure shows that having electron-beam polarization alone already makes a sizable improvement in sensitivity compared with no polarization at all (comparison of the ILC250♦ (*no pol.*) case and the first column of ILC250 in the plot). Adding positron-beam polarization enhances the sensitivity at low energies. However, at high energies, the positron-beam polarization becomes less critical. As observed in Fig. 1, the sensitivity depends on the polarization and increases with the $\sqrt{s}$. Including the ILC500 program in the ILC250 expectations allows the inspection of all studied GHU models up to the $B_2^\pm$ models, which predict $m_{KK} = 19$ TeV. Adding also the estimate for ILC1000, the discrimination of $B_3^\pm$ ($m_{KK} = 25$ TeV) will also be within reach.

5.3 The role of charged-hadron identification with the ILD TPC

In this study, we have assumed a novel TPC design that will allow cluster counting (dN/dx) for charged-hadron identification capabilities, with better resolution than using the mean energy loss per distance (dE/dx), described in detail in Sect. 3.3. We also consider two other scenarios: a first without any charged-hadron identification (although the TPC

---

[5] For simplicity we use 30% positron beam polarization also for the middle column for the ILC 1 TeV case. However, it is not the baseline configuration, which foresees 20% positron beam polarization.
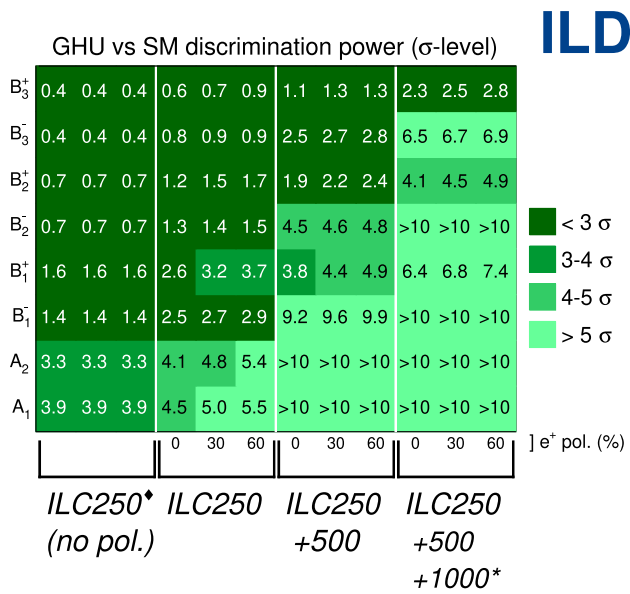
Fig. 5 Similar to Fig. 4 but fixing the R case for the Z-fermion couplings. Three scenarios for the positron beam polarization are shown. For the ILC250◆(*no pol.*) we continue assuming no polarization for any beam
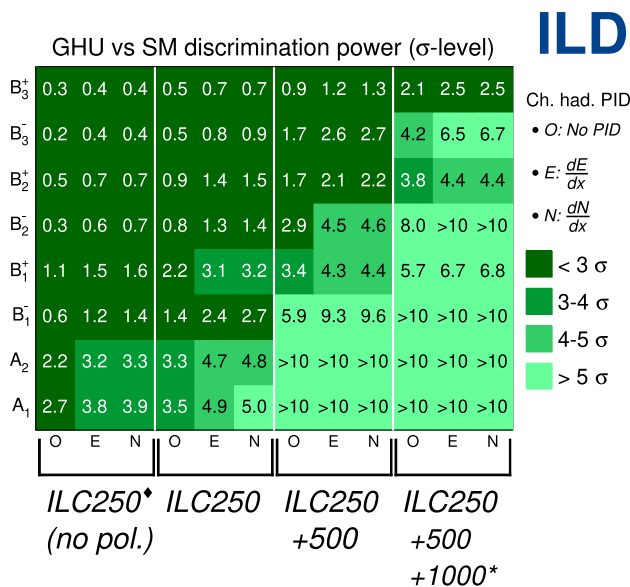

Fig. 6 Similar to Fig. 4 but fixing the R case for the Z-fermion couplings. Instead, three different scenarios for the charged hadron particle identification capabilities (PID) are considered: O for no PID used, E for PID based on the ILD baseline dE/dx reconstruction, and N for an optimized TPC design with higher granularity and cluster counting reconstruction dN/dx

tracking capabilities are still used for track reconstruction) and a second one using the traditional dE/dx for particle identification. In Ref. [21], it has been estimated that not using charged-hadron identification for the kaon selection could increase the statistical uncertainty by up to a factor of two, especially for the c-quark case, which largely relies on

the K-method, reducing the power of discovery of GHU in these signatures in the baseline program of ILC. The expectations for these three cases are shown in Fig. 6, assuming the R scenario for the Z couplings. The benefits of using charged-hadron identification capabilities with the ILD TPC become clear, especially at the lower energy stage of ILC, since it allows the use of two methods for charge determination, Vtx-method and K-method. The discrimination power differences between using dE/dx and dN/dx are moderate and depend on the different models: the ones predicting larger deviations for the c-quark case are more sensitive to moderate improvements in the K-method.

5.4 Discrimination power between GHU models

In Fig. 7, the statistical discrimination between the different GHU models is shown for different ILC scenarios. These four plots show the benefits of high longitudinal polarization for both beams and, especially, the benefits of the energy reach foreseen for the ILC. With operation at 500 GeV and above, almost full differentiation between the different models will be possible, allowing for detailed scrutiny of potential contributions from heavy resonances.

6 Summary and outlook

The search for new physics at the LHC and at future electron-positron colliders requires a global approach. Searching for new resonances is and will be addressed by a combination of direct searches for such resonances and the precise measurement of observables whose deviations with respect to SM predictions are sensitive to new physics. The ILC program will provide a broad range of experimental measurements that can be used to probe for BSM physics. The GHU models discussed here are especially sensitive to deviations in the electroweak observables at high $\sqrt{s}$ with polarized beams.

This study uses forward–backward asymmetries of b and c-quarks in high-energy electron-positron collisions to demonstrate the sensitivity to GHU-inspired models. The experimental input is based on detailed simulations of the ILD at center-of-mass energies of 250 and 500 GeV and extrapolated to 1000 GeV. More specifically, we present the fully differential cross-section $d\sigma/d\cos\theta$ from which the A_{FB}^b and A_{FB}^c are inferred. Studies at ILC250 and ILC500 have been completed, showing that a per-mil level of statistical precision is achievable. Experimental systematic uncertainties have been briefly discussed. These are found to be sub-dominant, thanks to: (a) the excellent vertexing and flavor-tagging capabilities expected at the ILC, (b) the use of fully differential measurements; and (c) the use of double-tagging and double-charge measurements that reduce the use
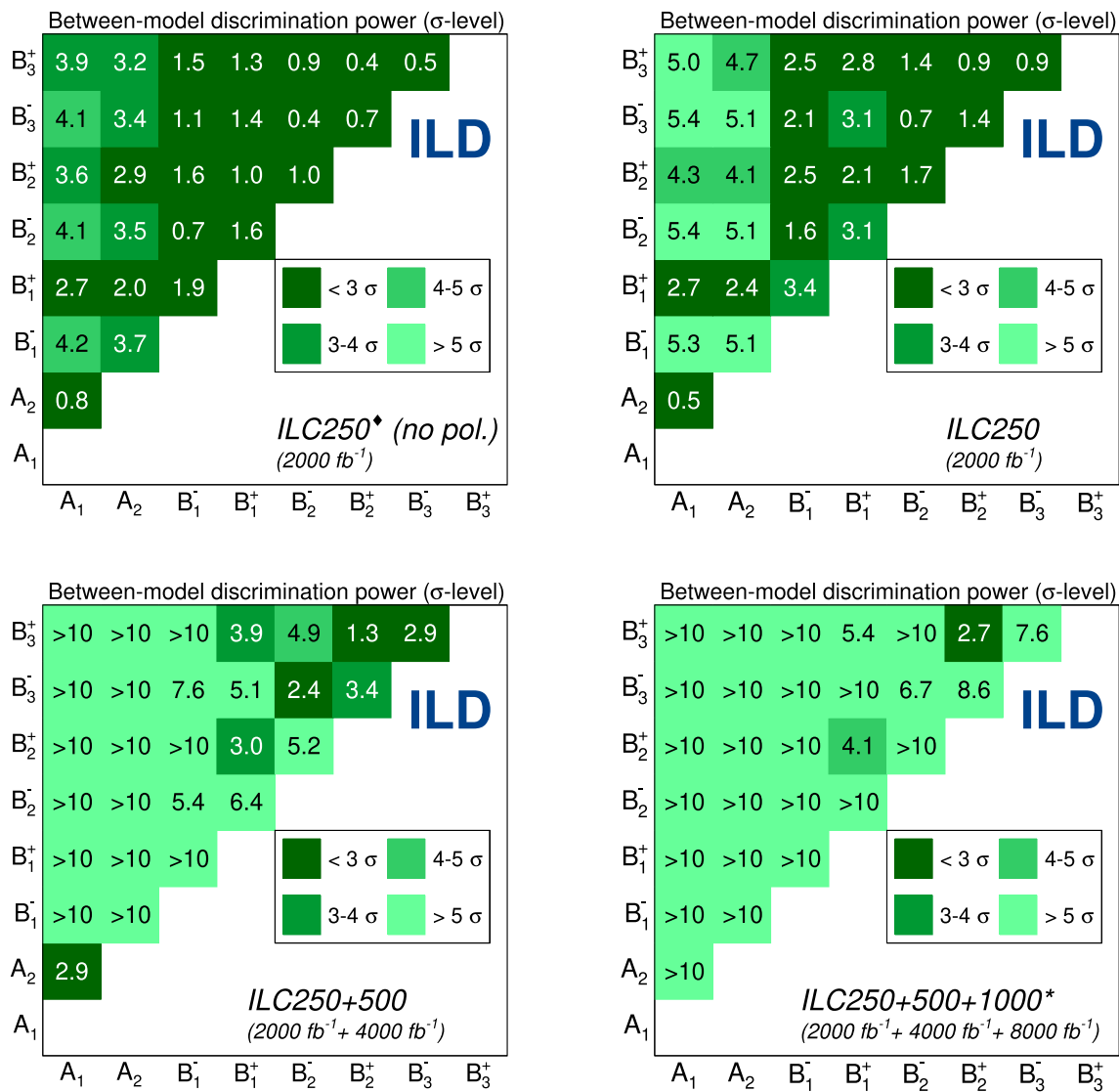
Fig. 7 Statistical discrimination power between GHU models after different ILC stages. For completeness, a hypothetical ILC250 stage assuming no longitudinal beam polarization is included. The ILC250♦(*no pol.*), ILC250, and ILC500 estimations are performed using full simulation studies. The ILC1000* is obtained from extrapolations of the ILC500 studies

of Monte Carlo tools to the minimum when addressing modeling uncertainties, such as the hadronization uncertainties.

Moreover, the ILD also offers the critical capability of providing charged-kaon identification over a broad momentum spectrum. This enhances the statistical efficiency of these measurements, and, in particular, it provides a factor ~ 2 improvement for A_{FB}^c. This analysis uses a simple approach based on selection cuts in kinematic distributions for the background rejection. Machine learning techniques like multi-classifying neural networks can improve the event selection and construct control regions for the backgrounds [67]. This will further improve the sensitivity of the analysis.

The analysis used currently available tools for tracking, vertexing, particle flow, jet reconstruction, and flavor tagging. In particular, the flavor-tagging algorithm is based on multivariate analysis using boosted decision trees as classifiers [49]. Advanced machine-learning methods such as graph neural networks are expected to significantly improve jet flavor identification performance [68].

The GHU models described in Refs. [27,29,31] show high expected sensitivity for the A_{FB}^b and A_{FB}^c observables. The expected sensitivity increases with the energy and depends on the electron and positron beam polarization. These GHU models predict new massive Z' resonances and deviations of all SM Z-fermion couplings. They are constructed not to induce significant changes in the EW precision observables

measured at past lepton colliders and agree with the non-observation of Z' at LHC.

We show that the ILC operating polarized beams colliding at 250 GeV and 500 GeV could provide full discrimination power (at the 5σ level) between these models and the SM, through A_{FB}^b and A_{FB}^c measurements. The ILC250 case has also been compared with an ILC250 without beam polarization. For the latter case, at least a factor of two of integrated luminosity is required to get similar prospects.

The ILC program also considers a run at high energies of 1000 GeV. Detailed studies of these scenarios, with optimized designs of the ILD, would be required to provide realistic estimations of the uncertainties expected in these cases. Instead, the exercise of extrapolating from the ILC500 full simulation studies has been performed. Including the predictions for ILC1000, full discovery potential for different GHU models predicting Kaluza-Klein resonance with masses up to 25 TeV will be possible.

It is important to remark on the intrinsic importance of precisely constraining the couplings of the Z-boson to all fermions without deviations caused by heavy resonances predicted by BSM. This can be done at dedicated runs at the Z-pole (ILCGigaZ) or with a dedicated analysis at ILC250 using radiative return events [64]. The importance of getting updated estimations for such couplings with at least one order of magnitude better precision than current measurements is also shown in this study.

This study is based on leading-order accurate simulations, and calculations should be updated, including next-to-leading order contributions in QCD and EW at the theory and Monte Carlo simulation level. This is out of the scope of this work due to the non-existence of such simulations or GHU predictions at the moment.

Measurements for different fermions, various types of observables, under different $\sqrt{s}$ and beam-polarization conditions will allow a deep investigation of such theories and the disentanglement of potential new effects: deviations of the Z-f couplings, contributions from new heavier resonances, mixing effects, etc. In particular, future colliders will provide multiple differential cross-section measurements for different processes that can be used to set limits on the SM via effective-field interpretation models. In the Standard Model Effective Field Theory (SMEFT) [69], the study of the implications of new physics is performed indirectly through the introduction of modifications to the SM at very high energies. The strength of the modification of SM couplings is determined by the energy scale at which the new physics is expected and the coupling strengths expressed by the Wilson coefficients, which can be fitted, or the exclusion limits on the SMEFT parameters and, therefore, BSM physics can be set. The SMEFT approach has the advantage of allowing the simulation of the impact of the modification of couplings for several physics processes simultaneously. Therefore, a global analysis of the data with different processes is possible, accounting for their correlations.

Data Availability Statement Data will be made available on reasonable request.

Code Availability Statement Code/software will be made available on reasonable request.

References

1. CMS Collaboration, S. Chatrchyan et al., Observation of a New Boson at a Mass of 125 GeV with the CMS experiment at the LHC. Phys. Lett. B **716**, 30–61 (2012). https://doi.org/10.1016/j.physletb.2012.08.021. arXiv:1207.7235 [hep-ex]

2. ATLAS Collaboration, G. Aad et al., Observation of a new particle in the search for the Standard Model Higgs boson with the ATLAS detector at the LHC. Phys. Lett. B **716**, 1–29 (2012). https://doi.org/10.1016/j.physletb.2012.08.020. arXiv:1207.7214 [hep-ex]

3. ALEPH, DELPHI, L3, OPAL, SLD, LEP Electroweak Working Group, SLD Electroweak Group, SLD Heavy Flavour Group, S. Schael et al., Precision electroweak measurements on the *z* resonance. Phys. Rep. **427**, 257–454 (2006). https://doi.org/10.1016/j.physrep.2005.12.006. arXiv:hep-ex/0509008

4. A. Djouadi, G. Moreau, F. Richard, Resolving the A(FB)**b puzzle in an extra dimensional model with an extended gauge structure. Nucl. Phys. B **773**, 43–64 (2007). https://doi.org/10.1016/j.nuclphysb.2007.03.019. arXiv:hep-ph/0610173

5. A. Accardi et al., Electron ion collider: the next QCD frontier: understanding the glue that binds us all. Eur. Phys. J. A **52**(9), 268 (2016). https://doi.org/10.1140/epja/i2016-16268-9. arXiv:1212.1701 [nucl-ex]

6. T. Behnke, J.E. Brau, B. Foster, J. Fuster, M. Harrison, J.M. Paterson, M. Peskin, M. Stanitzki, N. Walker, H. Yamamoto, The International Linear Collider Technical Design Report: Volume 1: Executive Summary. arXiv:1306.6327 [physics.acc-ph]

7. H. Baer et al., The International Linear Collider Technical Design Report: Volume 2: Physics. arXiv:1306.6352 [hep-ph]

8. C. Adolphsen et al., The International Linear Collider Technical Design Report: Volume 3.I: Accelerator & in the Technical Design Phase. arXiv:1306.6353 [physics.acc-ph]

9. C. Adolphsenc et al., The International Linear Collider Technical Design Report: Volume 3. II: Accelerator Baseline Design. arXiv:1306.6328 [physics.acc-ph]

10. H. Abramowicz et al., The International Linear Collider Technical Design Report: Volume 4: Detectors. arXiv:1306.6329 [physics.ins-det]

11. ILD Concept Group, H. Abramowicz et al., International large detector: interim design report. arXiv:2003.01116 [physics.ins-det]

12. CLIC, CLICdp Collaboration, M.J. Boland et al., Updated baseline for a staged Compact Linear Collider. arXiv:1608.07537 [physics.acc-ph]

13. CLIC Collaboration, J. de Blas et al., The CLIC potential for new physics. arXiv:1812.02093 [hep-ph]

14. CLICdp, CLIC Collaboration, T.K. Charles et al., The compact linear collider (CLIC): 2018 summary report. arXiv:1812.06018 [physics.acc-ph]

15. FCC Collaboration, A. Abada et al., FCC physics opportunities: future circular collider conceptual design report Volume 1. Eur. Phys. J. C **79**(6), 474 (2019). https://doi.org/10.1140/epjc/s10052-019-6904-3

16. FCC Collaboration, A. Abada et al., FCC-ee: the lepton collider: future circular collider conceptual design report volume 2. Eur. Phys. J. ST **228**(2), 261–623 (2019). https://doi.org/10.1140/epjst/e2019-900045-4

17. CEPC Study Group, CEPC Conceptual Design Report: Volume 1—Accelerator. arXiv:1809.00285 [physics.acc-ph]

18. CEPC Study Group, M. Dong et al., CEPC Conceptual Design Report: Volume 2—Physics & Detector. arXiv:1811.10545 [hep-ex]

19. C. Vernieri et al., Strategy for understanding the Higgs Physics: the cool copper collider. JINST **18**(07), P07053 (2023). https://doi.org/10.1088/1748-0221/18/07/P07053. arXiv:2203.07646 [hep-ex]

20. A. Irles, R. Pöschl, F. Richard, Experimental methods and prospects on the measurement of electroweak *b* and *c*-quark observables at the ILC operating at 250 GeV. arXiv:2306.11413 [hep-ex]

21. A. Irles, J.P. Marquez, Experimental prospects for precision observables in $e^-e^+ \to q\bar{q}$ with $q = b, c$ processes at the ILC operating at 250 and 500 GeV of center of mass, in *International Workshop on Future Linear Colliders*, vol. 7 (2023). arXiv:2307.14888 [hep-ex]

22. K. Agashe, R. Contino, A. Pomarol, The minimal composite Higgs model. Nucl. Phys. B **719**, 165–187 (2005). https://doi.org/10.1016/j.nuclphysb.2005.04.035. arXiv:hep-ph/0412089

23. A.D. Medina, N.R. Shah, C.E.M. Wagner, Gauge-Higgs unification and radiative electroweak symmetry breaking in warped extra dimensions. Phys. Rev. D **76**, 095010 (2007). https://doi.org/10.1103/PhysRevD.76.095010. arXiv:0706.1281 [hep-ph]

24. Y. Hosotani, K. Oda, T. Ohnuma, Y. Sakamura, Dynamical electroweak symmetry breaking in SO(5) x U(1) gauge-Higgs unification with top and bottom quarks. Phys. Rev. D

78, 096002 (2008). https://doi.org/10.1103/PhysRevD.78.096002. arXiv:0806.0480 [hep-ph] (Erratum: Phys. Rev. D 79, 079902 (2009))

25. S. Funatsu, H. Hatanaka, Y. Hosotani, Y. Orikasa, T. Shimotani, LHC signals of the $SO(5) \times U(1)$ gauge-Higgs unification. Phys. Rev. D **89**(9), 095019 (2014). https://doi.org/10.1103/PhysRevD.89.095019. arXiv:1404.2748 [hep-ph]

26. S. Funatsu, H. Hatanaka, Y. Hosotani, Y. Orikasa, N. Yamatsu, GUT inspired $SO(5) \times U(1) \times SU(3)$ gauge-Higgs unification. Phys. Rev. D **99**(9), 095010 (2019). https://doi.org/10.1103/PhysRevD.99.095010. arXiv:1902.01603 [hep-ph]

27. S. Funatsu, H. Hatanaka, Y. Hosotani, Y. Orikasa, N. Yamatsu, Fermion pair production at e^-e^+ linear collider experiments in GUT inspired gauge-Higgs unification. Phys. Rev. D **102**(1), 015029 (2020). https://doi.org/10.1103/PhysRevD.102.015029. arXiv:2006.02157 [hep-ph]

28. S. Funatsu, H. Hatanaka, Y. Hosotani, Y. Orikasa, N. Yamatsu, Signals of W' and Z' bosons at the LHC in the SU(3)×SO(5)×U(1) gauge-Higgs unification. Phys. Rev. D **105**(5), 055015 (2022). https://doi.org/10.1103/PhysRevD.105.055015. arXiv:2111.05624 [hep-ph]

29. S. Funatsu, H. Hatanaka, Y. Orikasa, N. Yamatsu, Single Higgs boson production at electron-positron colliders in gauge-Higgs unification. Phys. Rev. D **107**(7), 075030 (2023). https://doi.org/10.1103/PhysRevD.107.075030. arXiv:2301.07833 [hep-ph]

30. N. Yamatsu, S. Funatsu, H. Hatanaka, Y. Hosotani, Y. Orikasa, W and Z boson pair production at electron-positron colliders in gauge-Higgs unification. Phys. Rev. D **108**(11), 115014 (2023). https://doi.org/10.1103/PhysRevD.108.115014. arXiv:2309.01132 [hep-ph]

31. S. Funatsu, H. Hatanaka, Y. Hosotani, Y. Orikasa, Distinct signals of the gauge-Higgs unification in e^+e^- collider experiments. Phys. Lett. B **775**, 297–302 (2017). https://doi.org/10.1016/j.physletb.2017.10.068. arXiv:1705.05282 [hep-ph]

32. Y. Hosotani, N. Yamatsu, Gauge-Higgs grand unification. PTEP **2015**, 093B01 (2015). https://doi.org/10.1093/ptep/ptv153. arXiv:1504.03817 [hep-ph]

33. A. Furui, Y. Hosotani, N. Yamatsu, Toward realistic gauge-Higgs grand unification. PTEP **2016**(9), 093B01 (2016). https://doi.org/10.1093/ptep/ptw116. arXiv:1606.07222 [hep-ph]

34. P. Bambade et al., The international linear collider: a global project. arXiv:1903.01629 [hep-ex]

35. J.-C. Brient, H. Videau, The calorimetry at the future e+ e- linear collider. eConf **C010630**, E3047 (2001). arXiv:hep-ex/0202004

36. M.A. Thomson, Particle flow calorimetry and the PandoraPFA algorithm. Nucl. Instrum. Methods A **611**, 25–40 (2009). https://doi.org/10.1016/j.nima.2009.09.009. arXiv:0907.3577 [physics.ins-det]

37. LCTPC Collaboration, Y. Aoki et al., Double-hit separation and dE/dx resolution of a time projection chamber with GEM readout. JINST **17**(11), P11027 (2022). https://doi.org/10.1088/1748-0221/17/11/P11027. arXiv:2205.12160 [physics.ins-det]

38. M. Frank, F. Gaede, C. Grefe, P. Mato, DD4hep: a detector description toolkit for high energy physics experiments. J. Phys. Conf. Ser. **513**, 022010 (2014). https://doi.org/10.1088/1742-6596/513/2/022010

39. GEANT4 Collaboration, S. Agostinelli et al., GEANT4: a simulation toolkit. Nucl. Instrum. Methods A **506**, 250–303 (2003). https://doi.org/10.1016/S0168-9002(03)01368-8

40. J. Allison et al., Geant4 developments and applications. IEEE Trans. Nucl. Sci. **53**, 270 (2006). https://doi.org/10.1109/TNS.2006.869826

41. J. Allison et al., Recent developments in Geant4. Nucl. Instrum. Methods A **835**, 186–225 (2016). https://doi.org/10.1016/j.nima.2016.06.125

42. W. Kilian, T. Ohl, J. Reuter, WHIZARD: simulating multi-particle processes at LHC and ILC. Eur. Phys. J. **C71**, 1742 (2011). https://doi.org/10.1140/epjc/s10052-011-1742-y. arXiv:0708.4233 [hep-ph]

43. T. Sjöstrand, S. Mrenna, P. Skands, Pythia 6.4 physics and manual. J. High Energy Phys. **2006**(05), 026 (2006). https://doi.org/10.1088/1126-6708/2006/05/026

44. D. Schulte, Beam-beam simulations with Guinea-Pig. eConf **C980914**, 127–131 (1998). https://www.slac.stanford.edu/econf/C980914/papers/F-Th24.pdf

45. P. Chen, T. L. Barklow, M. E. Peskin, Hadron production in collisions as a background for linear colliders. Phys. Rev. D **49**(7), (1994). https://doi.org/10.1103/physrevd.49.3209

46. LCC Collaboration, M. Berggren, Generating the full SM at linear colliders. PoS **ICHEP2020**, 903 (2021). https://doi.org/10.22323/1.390.0903. arXiv:2105.04049 [hep-ex]

47. F. Gaede, S. Aplin, R. Glattauer, C. Rosemann, G. Voutsinas, Track reconstruction at the ILC: the ILD tracking software. J. Phys. Conf. **513**(2), 022011 (2014). https://doi.org/10.1088/1742-6596/513/2/022011

48. J.S. Marshall, M.A. Thomson, The pandora software development kit for pattern recognition. Eur. Phys. J. C **75**(9), 439 (2015). https://doi.org/10.1140/epjc/s10052-015-3659-3. arXiv:1506.05348 [physics.data-an]

49. T. Suehara, T. Tanabe, LCFIPlus: a framework for jet analysis in linear collider studies. Nucl. Instrum. Methods A **808**, 109–116 (2016). https://doi.org/10.1016/j.nima.2015.11.054. arXiv:1506.08371 [physics.ins-det]

50. M. Boronat, J. Fuster, I. Garcia, P. Roloff, R. Simoniello, M. Vos, Jet reconstruction at high-energy electron–positron colliders. Eur. Phys. J. C **78**(2), 144 (2018). https://doi.org/10.1140/epjc/s10052-018-5594-6. arXiv:1607.05039 [hep-ex]

51. J. Kennedy, R. Eberhart, Particle swarm optimization. in *Proceedings of ICNN'95: International Conference on Neural Networks*, vol. 4 (1995), p. 1942–1948. https://doi.org/10.1109/ICNN.1995.488968

52. A. Kolmogorov, Sulla determinazione empirica delle leggi di probabilita. Giorn. Ist. Ital. Attuari **4**, 1–11 (1933)

53. N. Smirnov, Table for estimating the goodness of fit of empirical distributions. Ann. Math. Stat. **19**(2), 279–281 (1948)

54. J. Hodges Jr., The significance probability of the smirnov two-sample test. Arkiv för Mat. **3**(5), 469–486 (1958)

55. T.W. Anderson, D.A. Darling, Asymptotic theory of certain "goodness of fit" criteria based on stochastic processes. Ann. Math. Stat. **23**(2), 193–212 (1952). http://www.jstor.org/stable/2236446

56. T.W. Anderson, D.A. Darling, A test of goodness of fit. J. Am. Stat. Assoc. **49**(268), 765–769 (1954)

57. S. Engmann, D. Cousineau, Comparing distributions: the two-sample Anderson–Darling test as an alternative to the Kolmogorov–Smirnoff test. J. Appl. Quant. Methods **6**(3), (2011). https://doi.org/10.1007/s10958-017-3638-3

58. S. Bilokin, Hadronic showers in a highly granular silicon-tungsten calorimeter and production of bottom and top quarks at the ILC, tel-01946099

59. T. Mizuno, Photon energy calibration using $e^-e^+ \to \gamma Z$ at the ILC. ILD-PHYS-PUB-2019-006

60. J. de Blas, et al., Focus topics for the ECFA study on Higgs / Top / EW factories. arXiv:2401.07564 [hep-ex]

61. J.A. Maestre, Revisiting QCD corrections to the forward-backward charge asymmetry of heavy quarks in electron–positron collisions at the Z pole: really a problem? arXiv:2010.08604 [hep-ph]

62. R. Karl, *From the Machine-Detector Interface to Electroweak Precision Measurements at the ILC: Beam-Gas Background, Beam Polarization and Triple Gauge Couplings*. Ph.D. dissertation, Universität Hamburg, Hamburg (2019). https://doi.org/10.3204/PUBDB-2019-03013

63. Particle Data Group, P.A. Zyla et al., Review of particle physics. PTEP **2020**(8), 083C01 (2020). https://doi.org/10.1093/ptep/ptaa104

64. ILC International Development Team, A. Aryshev et al., The International Linear Collider: Report to Snowmass 2021. arXiv:2203.07622 [physics.acc-ph]

65. A. Irles, R. Poeschl, F. Richard, H. Yamamoto, Complementarity between ILC250 and ILC-GigaZ, in *Linear Collider Community Meeting Lausanne, Switzerland, April 8-9, 2019* (2019). arXiv:1905.00220 [hep-ex]

66. Positron Working Group, W. Gai et al., Report on the ILC positron source. https://edmsdirect.desy.de/item/D00000001165115

67. CMS Collaboration, A.M. Sirunyan et al., Search for t$\bar{\text{t}}$H production in the H $\to$ b$\bar{\text{b}}$ decay channel with leptonic t$\bar{\text{t}}$ decays in proton-proton collisions at $\sqrt{s} = 13$ TeV. JHEP **03**, 026 (2019). https://doi.org/10.1007/JHEP03(2019)026. arXiv:1804.03682 [hep-ex]

68. ATLAS Collaboration, Graph Neural Network Jet Flavour Tagging with the ATLAS Detector. ATL-PHYS-PUB-2022-027

69. I. Brivio, M. Trott, The Standard Model as an effective field theory. Phys. Rep. **793**, 1–98 (2019). https://doi.org/10.1016/j.physrep.2018.11.002. arXiv:1706.08945 [hep-ph]